



Published in final edited form as:

ACS Appl Mater Interfaces. 2019 November 27; 11(47): 43879–43887. doi:10.1021/acsami.9b15195.

Ultrasmall Renally Clearable Silica Nanoparticles Target Prostate Cancer

Feng Chen^{†, #}, Kai Ma^{‡, #}, Li Zhang[†], Brian Madajewski[†], Melik Z. Turker[‡], Fabio Gallazzi[§], Kiara Cruickshank[†], Xiuli Zhang^{||}, Pocharapong Jenjitrant[†], Karim A. Touijer[⊥], Thomas P. Quinn^{||, ■}, Pat Zanzonico[●], Ulrich Wiesner^{*, ‡}, Michelle S. Bradbury^{*, †, ▲}

[†]Department of Radiology, Sloan Kettering Institute for Cancer Research, New York, New York 10065, United States

[▲]Molecular Pharmacology Program, Sloan Kettering Institute for Cancer Research, New York, New York 10065, United States

[‡]Department of Materials Science & Engineering, Cornell University, Ithaca, New York 14853, United States

[§]Department of Chemistry and Molecular Interactions Core, University of Missouri, Columbia, Missouri 65211, United States

^{||}Department of Biochemistry, University of Missouri, Columbia, Missouri 65211, United States

[⊥]Urology Service, Department of Surgery, Memorial Sloan Kettering Cancer Center, New York, New York 10065, United States

[●]Department of Medical Physics, Memorial Sloan Kettering Cancer Center, New York, New York 10065, United States

[■]Harry S Truman Veterans' Hospital, Columbia, Missouri 65201, United States

Abstract

Although important advances have been achieved in the development of radiolabeled prostate-specific membrane antigen (PSMA)-targeting ligand constructs for both diagnosis and therapy of prostate cancer (PCa) over the past decade, challenges related to off-target effects and limited treatment responses persist. In this study, which builds upon the successful clinical translation of a

*Corresponding Authors: bradburm@mskcc.org (M.S.B.). ubw1@cornell.edu (U.W.).

#F.C. and K.M. contributed equally to this work.

Author Contributions

The manuscript was written through contributions of all authors. All authors have given approval to the final version of the manuscript.

Supporting Information

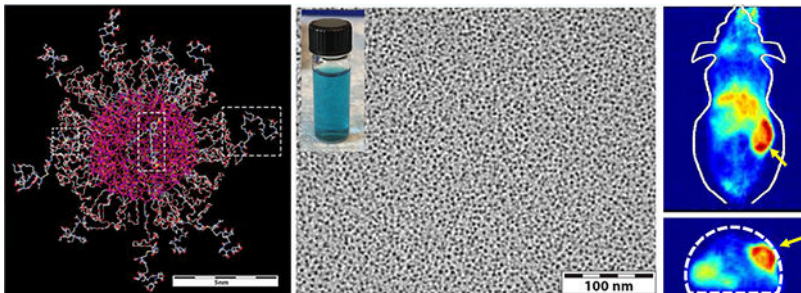
The Supporting Information is available free of charge on the ACS Publications website at DOI: 10.1021/acsami.9b15195.

Schematic illustration of the core-shell structure of the ultrasmall silica-based PSMA-targeting PET/optical dual-modality nanoparticles; schematic illustration of the synthesis of the native PSMAi peptid; schematic illustration of the synthesis of PSMAi-PEG-silane and Cy5-silane; IC₅₀ comparison between DFO-PSMAi-PEG-Cy5.5-C' dots and the native PSMAi peptide; representative PD-10 elution profile of ⁸⁹Zr-DFO-PSMAi-PEG-Cy5-C' dots; biodistribution of ⁸⁹Zr-DFO-PSMAi-PEG-Cy5-C' dots in major organs and tissues in normal, healthy mice; correlative ex vivo tumor histopathology; cumulative clearance of ⁸⁹Zr-DFO-PSMAi-PEG-Cy5-C' dots in mouse urine and feces at different postinjection time points; ex vivo biodistribution data of ⁸⁹Zr-DFO-PSMAi-PEG-Cy5-C' dots; radiation dosimetry of ⁸⁹Zr-DFO-PSMAi-PEG-Cy5-C' dots (PDF)

The authors declare the following competing financial interest(s): M.S.B. and U.W. hold interest in Elucida Technologies, Inc., which has licensed IP from Cornell and MSKCC on C dots and their application in oncology.

series of ultrasmall, dye-encapsulating core-shell silica nanoparticles, or Cornell Prime Dots (C' dots), for cancer management, we sought to address these limitations by designing a dual-modality, PSMA-targeting platform that evades undesirable accumulations in the salivary glands, kidneys, and reticuloendothelial system, while exhibiting bulk renal clearance. This versatile PCa-targeted particle imaging probe offers significant clinical potential to improve future theranostic applications in a variety of patient care settings.

Graphical Abstract



Keywords

ultrasmall; C' dots; PSMA; prostate cancer; targeting

INTRODUCTION

Noninvasive, high-sensitivity, whole-body positron emission tomography (PET)-computerized tomography (CT) imaging plays a vital role in tumor staging, treatment planning, and response monitoring of many malignant tumors, including prostate cancer (PCa). As the second leading cause of cancer-related diseases among men in the United States, there have been an estimated 174 650 new cases of PCa and 31 620 deaths in 2019 alone^{1,2,3} A large proportion of these cancers overexpress a type-II transmembrane glycoprotein, prostate-specific membrane antigen (PSMA), at a level that is 100- to 1000-fold greater than that found in normal tissues.⁴ PSMA is a highly attractive molecular target for both diagnostic and therapeutic applications in patients with biochemical recurrence (BCR).⁵ However, most reported PSMA-based probes for human use have only been formulated as single-modality PET imaging agents, offering relatively coarse spatial resolution (5–6 mm) and no higher-resolution optical imaging capabilities for image-guided surgery. The development of such a novel and clinically translatable dual-modality (PET-optical), PSMA-targeting imaging platform—one that also exhibits bulk renal clearance while showing substantial reductions in salivary gland, renal, and hepatic (or reticuloendothelial system, RES) uptake—is paradigm-shifting, and remains a critical unmet need of PCa care.

Important advances have been made toward developing a variety of PSMA-targeting ligand constructs, such as monoclonal antibodies [mAb],⁶ antibody fragments,⁷ and urea-based small-molecule inhibitors,^{8,9} labeled with either diagnostic (i.e., gallium-68 [⁶⁸Ga, $t_{1/2}$ = 68 min], fluorine-18 [¹⁸F; $t_{1/2}$ = 110 min], zirconium-89 [⁸⁹Zr; $t_{1/2}$ = 78 h]) positron-emitting radionuclides or therapeutic (i.e., lutetium-177 [¹⁷⁷Lu, $t_{1/2}$ = 6.6 days], actinium-225 [²²⁵Ac;

$t_{1/2} = 10$ days]) β -particle- or α -particle-emitting radionuclides. However, challenges related to nonspecific tissue accumulations, off-target toxicities, and/or limited treatment responses, among others, restricting application of such agents in humans, remain.

In particular, the prolonged blood circulation half-life and poor solid-tumor penetration properties of radiolabeled PSMA-targeting intact antibodies (e.g., ^{89}Zr -DFO-J591^{6,10,11}) can lead to reduced diagnostic accuracy in light of the high background signal that may obscure metastatic lesions, as well as unacceptable marrow toxicity during radiotherapy.^{12,13} By contrast, urea-based small-molecule inhibitors have shown significantly improved renal clearance profiles when compared to mAbs.^{3,12} However, reduced diagnostic performance associated with the relatively shorter half-life of such ^{68}Ga -labeled constructs have limited postinjection (p.i.) imaging times to within 1–2 h, often at times of high urinary bladder activity. Even given the availability of state-of-the-art hospital PET/CT scanners, the high cost of maintaining an in-house $^{69}\text{Ge}/^{68}\text{Ga}$ generator, along with the short decay half-life, make it impractical to ship ^{68}Ga -labeled, PSMA-targeting PET probes even short distances, causing distribution challenges with the rising demand of such probes. Finally, although relatively mild nonhematologic toxicity has been reported for ^{177}Lu -PSMA-based radiotherapy, the high off-target uptake that occurs in radiosensitive organs (i.e., salivary glands) with ^{177}Lu - or ^{225}Ac -PSMA-617 continue to raise toxicity concerns.^{14,15}

In this work, we build upon the successful clinical translation of a series of ultrasmall and renally cleared fluorescent core-shell silica nanoparticles, Cornell Prime Dots (C' dots), for targeted PET and/or optical detection of metastatic melanoma (Clinical Trials [NCT01266096](#) and [NCT03465618](#)) and malignant brain tumors ([NCT02106598](#)). We present the development of a first-in-kind ultrasmall (sub-8 nm) PSMA-targeting C' dot for dual-modality imaging in preoperative (PET) and/or intraoperative (optical) settings. In addition to overcoming the aforementioned limitations of other targeted PET agents for PCa care, the favorable physicochemical and biological properties of this platform lay the foundation for targeted chemo- and radiotherapeutic applications.

EXPERIMENTAL SECTION

Synthesis and Characterization of PSMA Inhibitor (PSMAi) Peptides (Scheme S2).

The PSMAi peptide was produced using standard fluorenylmethoxycarbonyl (Fmoc) solid-phase peptide synthesis (SPPS) chemistry on an APEX-396 or Tetras (Advanced ChemTech) multiple peptide synthesizer. Initially, the PSMA-targeting pharmacophore was synthesized by loading 2ClTrt-resin (Trt: trityl) with Fmoc-NH-Lys(Dde)-OH to yield **Compound 1**, Fmoc-NH-Lys(Dde)-CO-2ClTrt-resin (Dde: 1-(4,4-dimethyl-2,6-dioxacyclohexylidene)ethyl). Concurrently, $\text{NH}_2\text{-Glu}(\text{OtBu})_2$ was reacted with triphosgene and DIEA (DIEA: *N,N*-diisopropylethylamine) for 6 h at 0 °C to produce OCN-Glu-(OtBu)₂. The Fmoc protecting group was orthogonally removed from the Fmoc-NH-Lys(Dde)-CO-2ClTrt-resin (20% piperdine) and an overnight reaction at room temperature between the isocyanate building block [OCN-Glu-(OtBu)₂] and the free α -amino group of **Compound 1** yielded the fully protected urea-linked PSMAi pharmacophore **Compound 2** on the resin. The Lys(Dde) side-chain protecting group of **Compound 2** was removed with 2% hydrazine followed by the addition of the peptidic linker sequence Ac-Cys-Ahx-Ahx-

dLys-Ahx (Ac-: acetyl; Ahx: 6-aminohexanoic acid; Cys: cysteine) to the ϵ -amino group of the Lys using SPPS to yield **Compound 3**. The dLys residue was inserted in the peptidic linker as a site for future modification. The target peptide **Compound 4** was cleaved from the resin and the side-chain protecting groups removed from **Compound 3** by treating it with trifluoroacetic acid (TFA), in the presence of the following scavengers at 2.5% concentration each: Phenol, water, triisopropylsilane (TIS), thioanisole (TA) and ethanedithiol (EDT), followed by ether precipitation. The peptide precipitant was dissolved in a 50:50 mixture of water/acetonitrile and lyophilized.

The PSMAi peptide was characterized by liquid chromatography-mass spectroscopy (LC-MS) and finally purified by mass spectroscopy (MS) aided semipreparative high-performance liquid chromatography, using a water/acetonitrile (0.1% TFA) gradient. The calculated mass over charge (m/z) ratio for the PSMAi peptide ($m/z = 931.5$) and the experimentally determined value ($m/z = 932.4$) were in good agreement. The final PSMAi peptide product was stored as a lyophilized powder at $-20\text{ }^{\circ}\text{C}$.

Conjugation of PSMAi-Poly(ethylene glycol) (PEG)-Silane and Cy5-Silane (Scheme S3).

For the conjugation of PSMAi-PEG-silane, cysteine-PSMAi ligand and heterobifunctional PEG (mal-dPEG@12-NHS, Quantum Biodesign) were first separately dissolved in dimethyl sulfoxide (DMSO) under nitrogen at a concentration of around 0.021 and 1.2 M, respectively. mal-dPEG@12-NHS/DMSO solution was then mixed with 3-triethoxysilylpropylamine (APTES, liquid) under nitrogen at a molar ratio of 1:0.9 (mal-dPEG@12-NHS/APTES). The mixture was left under nitrogen overnight to conjugate the mal-dPEG@12-NHS molecule with a silane group via amine-NHS ester reaction forming mal-PEG-silane. After that, cysteine-PSMAi/DMSO solution was further added at a molar ratio of 1.1:1:0.9 (cysteine-PSMAi/mal-dPEG@12-NHS/APTES). The mixture was then left under nitrogen overnight, forming PSMAi-PEG-silane via thiol-ene click reaction. For the conjugation of Cy5-silane, Cy5-maleimide (Cy5-mal) was first dissolved in DMSO at a concentration of 0.1 mg/mL. Cy5-mal was then mixed with (3-mercaptopropyl)trimethoxysilane (MPTMS, liquid) at a molar ratio of 1:25 (Cy5-mal/MPTMS). The mixture was left under nitrogen overnight, forming Cy5-silane via thiol-ene click reaction.

Synthesis and Characterization of Ultrasmall Deferoxamine (DFO)-PSMAi-PEG-Cy5-C' Dots.

To synthesize ultrasmall DFO-PSMAi-PEG-Cy5-C' dots, we added around $30\text{ }\mu\text{L}$ of the conjugated Cy5-silane/DMSO precursor solution together with $68\text{ }\mu\text{L}$ of tetramethyl orthosilicate (TMOS) into 10 mL of deionized (DI) water at pH between 7.5 and 8.5. The reaction mixture was stirred at room temperature overnight, followed by addition of $100\text{ }\mu\text{L}$ of PEG-silane (Gelest, MW around 500) and $150\text{ }\mu\text{L}$ of the conjugated PSMAi-PEG-silane/DMSO precursor solution, followed by heat treatment at $80\text{ }^{\circ}\text{C}$ overnight. As-synthesized PSMAi-PEG-Cy5-C' dots were surface-functionalized with amine groups by reacting with amine-saline, forming NH_2 -PSMAi-PEG-Cy5-C' dots. The resulting NH_2 -PSMAi-PEG-Cy5-C' dots were purified by gel permeation chromatography (GPC) and sterile-filtered for characterization by GPC, fluorescence correlation spectroscopy (FCS), UV-vis absorption

and emission spectroscopy, and transmission electron microscopy (TEM). A Biologic LP system (Biorad) equipped with a 275 nm UV detector and a self-packed column (Superdex 200 resin, GE Healthcare Life Science) were used for GPC purification and characterization. A custom-built multichannel FCS setup was used for the characterization of particle concentration and hydrodynamic size.¹⁶ FCS results together with UV-vis spectroscopy results were used to determine the number of Cy5 dyes and PSMAi-targeting ligands per C' dot. UV-vis absorbance spectra were measured on a Cary 5000 spectrophotometer (Agilent). TEM images were taken on a T12 Spirit electron microscope (FEI).

To conjugate the nanoparticles with DFO (surface density: 3–5 DFO per particle) for PET imaging, we mixed NH₂-PSMAi-PEG-Cy5-C' dots with DFO-NCS (molar ratio of 1:20) for 1–2 h at room temperature and pH 8–9 under shaking (640 rpm). Unreacted DFO was removed through a PD-10 column using phosphate-buffered saline (PBS) as the mobile phase.

In Vitro PSMA Targeting of Ultrasmall C' Dots.

LNCap and PC-3 cells were plated in full growth media at a density of 5×10^5 cells/well in six-well culture plates. Cells were allowed to attach overnight, after which time the media were removed and replaced with growth media containing DFO-PSMAi-PEG-Cy5-C' dots at concentrations ranging from 0 to 100 nM. Cells were incubated with DFO-PSMAi-PEG-Cy5-C' dots for 4 h at 37 °C. After incubation, culture media were removed, and cells were washed two times with PBS followed by trypsinization. Trypsin was then neutralized with excess full growth media and the cell suspension was centrifuged at 1500 rpm for 3 min. The cell pellets were again washed with PBS and centrifuged, and the supernatant was removed. The cell pellets were then suspended in flow buffer containing 0.05 mg/mL 4',6-diamidino-2-phenylindole (DAPI) for live/dead cell determination. Samples were analyzed on a LSRFortessa flow cytometer (BD Biosciences) and results were displayed as median fluorescence intensity values.

In Vitro Competitive Binding Studies.

The IC₅₀ (concentration of peptide required to inhibit 50% of radioligand binding) was determined for DFO-PSMAi-PEG-Cy5.5-C' dots and PSMAi peptide in competitive binding assays with purified ⁶⁷Ga[1,4,7-triazacyclononane-1,4,7-triacetic acid (NOTA)]-PSMAi-PEG-Cy5.5-C' dots. LNCap cells were plated at a density of 0.2 million/well in 24-well tissue culture plates and incubated overnight. Individual wells were incubated at 25 °C for 2 h with approximately 50 000 cpm ⁶⁷Ga-(NOTA)-PSMAi-PEG-Cy5.5-C' dots in 0.3 mL of binding medium [Dulbecco's modified Eagle's medium with 25 mM N-(2-hydroxyethyl)-piperazine-N'-(2-ethanesulfonic acid) (HEPES), pH 7.4, 0.02% bovine serum albumin (BSA), and 0.3 mM 1,10-phenanthroline] with concentrations of DFO-PSMAi-PEG-Cy5.5-C' dots and PSMAi peptide ranging from 10⁻¹³ to 10⁻⁶ mol/L. The binding media was aspirated after incubation. Cells were rinsed with 0.5 mL of ice-cold pH 7.1, 0.02% BSA/0.01 M PBS twice and lysed with 0.5 mL of 1 M NaOH for 10 min. The cell lysate was collected and radioactivity measured in a γ -counter. The IC₅₀ values of DFO-PSMAi-PEG-Cy5.5-C' dots and PSMAi peptide were calculated with GraphPad Prism version 7.03.

⁸⁹Zr Radiolabeling of DFO-PSMAi-PEG-Cy5-C' Dot.

For chelator-based ⁸⁹Zr labeling, 0.75 nmol of DFO-PSMAi-PEG-Cy5-C' dots were mixed with 1 mCi of ⁸⁹Zr-oxalate in HEPES buffer (pH 8) at 37 °C for 60 min; final labeling pH was kept at 7–7.5. The labeling yield could be monitored by using radio instant thin-layer chromatography (iTLC). An ethylenediaminetetraacetic acid (EDTA) challenge procedure was then introduced to remove any nonspecifically bound ⁸⁹Zr from the particle surface. As-synthesized ⁸⁹Zr-DFO-PSMAi-PEG-Cy5-C' dots were then purified by using a PD-10 column (Figure S2). The final radiochemical purity was quantified by using iTLC.

In Vitro Radiostability Studies.

To study in vitro radiostability, we put ⁸⁹Zr-DFO-PSMAi-PEG-Cy5-C' dots in PBS (1×), as well as human and mouse serum, at 37 °C under shaking (650 rpm). Radiochemical purity was measured over a 6-day period by iTLC at various time points from the end of synthesis. The radiochemical purity at each time point was quantified by using iTLC.

Renal and Hepatic Clearance.

To study the renal and hepatic clearance of ⁸⁹Zr-DFO-PSMAi-PEG-Cy5-C' dots, we injected each healthy mouse (6–8 week old male NOD.CB17-Prkdc^{SCID}/J) with about 50 μCi (1.85 MBq) of ⁸⁹Zr-DFO-PSMAi-PEG-Cy5-C' dots. Each animal was individually housed in its own metabolic cage. Urine and fecal radioactivity were separately measured over a range of postinjection time points (i.e., 4, 24, 48, 72, 120, and 168 h) using a CRC-55tR Dose Calibrator, and presented as %ID (mean ± SD).

Animal Models and Tumor Inoculation.

LNCap prostate tumor xenografts were created by the subcutaneous injection of 1×10^7 cells into the right flank of 6–8 week old male NOD.CB17-Prkdc^{SCID}/J mice (Jackson Laboratories, Bar Harbor, ME). PC-3 prostate tumor xenografts were generated by subcutaneously injecting 6–8 week old male NOD.CB17-Prkdc^{SCID}/J mice with 2×10^6 cells in the right flank. Injections of both LNCaP and PC-3 cell lines were performed in a 50:50 mixture of PBS and Matrigel in a total volume of 100 μL. Mice were monitored for tumor growth over time, and all subsequent studies were initiated when tumors reached an average volume of 100 mm³ as determined by caliper measurements. All animal experiments were done in accordance with protocols approved by the Institutional Animal Care and Use Committee of Memorial Sloan Kettering Cancer Center and NIH guidelines for animal welfare were followed.

Dosimetry.

Radio dosimetry was calculated by using the OLINDA dosimetry program¹⁷ and following the procedures reported previously.²⁴

In Vivo PET Imaging and Ex Vivo Biodistribution Studies.

In vivo prostate cancer targeted PET imaging and ex vivo biodistribution studies were performed by using similar procedures we reported previously.²⁴

Statistics.

All comparisons were performed using a two-sample *t*-test based on three/five replications.

RESULTS AND DISCUSSION

As shown in Scheme 1A and Scheme S1, the core of this nanoparticle, an amorphous silica matrix, was designed to encapsulate a variety of deep/near-infrared organic dyes (i.e., Cy5, Cy5.5, cw800, etc.). The optical properties of the silica core facilitate measurements of (i) key physicochemical parameters, including particle size (nm) and concentration (nM), by fluorescence correlation spectroscopy (FCS) and, concomitantly, (ii) *in vitro* cell binding and internalization, and (iii) *in vivo* targeted uptake in cancerous tissues with *ex vivo* histologic correlation, using either small-animal imaging devices or imaging-guided surgical tools for larger animal models and human subjects. The physical size of the core is carefully controlled in water-based environments to be ~4 nm using a well-established C' dot synthesis technique.¹⁸ The silica core is subsequently covered by a functional shell, which is comprised of (i) a protective PEG (MW ~500 g/mol) layer to prevent the silica core from aggregating in water (or other media) during storage or circulation in the bloodstream, (ii) PSMAi for active PCa targeting, and (iii) radionuclide chelators, such as DFO, NOTA, or 1,4,7,10-tetraazacyclododecane-1,4,7,10-tetraacetic acid for radiolabeling with ⁸⁹Zr, ⁶⁴Cu, or ¹⁷⁷Lu/²²⁵Ac, respectively.

A modified water-based approach was introduced for the synthesis of ultrasmall DFO-PSMAi-PEG-Cy5-C' dots,^{18–20} informed by earlier results in alcohol.^{21,22} PSMAi, PSMAi-PEG-silane, and Cy5-silane (Schemes S2 and S3) were presynthesized prior to particle synthesis. As shown in Scheme 1B, Cy5-silane was first reacted with tetramethyl orthosilicate (TMOS) in deionized (DI) water (or other media) at room temperature, with the pH adjusted to ~8, to form Cy5-C' dots. PEGylation and peptide-functionalization steps were then introduced by adding PEG-silane and PSMAi-PEG-silane precursors and reacted at room temperature before overnight heat treatment at 80 °C to form PSMAi-PEG-Cy5-C' dots.¹⁹

To facilitate additional bioconjugation reactions, we surface-functionalized PSMAi-PEG-Cy5-C' dots with additional amine groups by reacting them with amine-silanes to form NH₂-PSMAi-PEG-Cy5-C' dots.²⁰ The reaction solution was cooled to room temperature, purified by GPC, and sterile-filtered. Purified NH₂-PSMAi-PEG-Cy5-C' dots were mixed with *p*-SCN-Bn-deferoxamine (DFO-NCS) (molar ratio 1:20) for 1–2 h at room temperature (pH 8–9) under shaking, to form DFO-PSMAi-PEG-Cy5-C' dots (3–5 DFO per C' dot). Finally, ⁸⁹Zr was added to create ⁸⁹Zr-DFO-PSMAi-PEG-Cy5-C' dots. Unreacted DFO or free ⁸⁹Zr was removed with a PD-10 column and PBS as the mobile phase.

Similar to prior reports detailing the characterization of ultrasmall Cy5-encapsulating C' dots,^{18,19,23–26} the UV-vis spectra of GPC-purified NH₂-PSMAi-PEG-Cy5-C' dots exhibited strong absorption at a wavelength of ~650 nm, which corresponded to the absorption maximum of Cy5 fluorescent dye (Figure 1A). The number of PSMAi ligands and Cy5 dyes per C' dot was estimated to be approximately 10 and 1.8, respectively.²³ The average hydrodynamic diameter of the purified NH₂-PSMAi-PEG-Cy5-C' dots measured

6.2 nm (Figure 1B). The GPC elugram of the NH₂-PSMAi-PEG-Cy5-C' dots showed a single peak at around 9 min, corresponding to the particle probe (Figure 1C).^{18,19,23} The peak could be well fit by a single Gaussian distribution, suggesting nearly 100% purity, and exhibited a narrow size distribution (Figure 1a).^{23,25} Representative TEM and photographic images (under natural light) of blue-colored NH₂-PSMAi-PEG-Cy5-C' dots in water are seen in Figure 1D (left and middle). Figure 1D (right) illustrates the different emission intensities between NH₂-PSMAi-PEG-Cy5-C' dots and water (control), acquired using an excitation wavelength of 640 nm in the IVIS Spectrum in vivo imaging system; these images illustrate the optical imaging capabilities of the particles.

After conjugating DFO-NCS (or p-SCN-Bn-deferoxamine) to NH₂-PSMAi-PEG-Cy5-C' dots, we tested the PSMA-targeting efficiency of nonradiolabeled DFO-PSMAi-PEG-Cy5-C' dots and the in vitro stability of radiolabeled ⁸⁹Zr-DFO-PSMAi-PEG-Cy5-C' dots. PSMA-specific targeting was observed (Figure 1E) in LNCap cells, a high-PSMA-expressing cell line. These cells demonstrated significantly enhanced uptake of DFO-PSMAi-PEG-Cy5-C' dots relative to that found for PC-3 cells (controls), which are known to express a modest, but finite, number of PSMA proteins on the cell surface (~14 000 per PC-3 cell), as against ~105 000 PSMA proteins per LNCap cell.²⁷ The PC-3 cell line therefore expresses PSMA protein at a level greater than 10% of that in the LNCap cell line and, thus, is not an absolute negative control for a PSMA-targeted agent. The observed uptake of DFO-PSMAi-PEG-Cy5-C' dots by PC-3 cells is, therefore, not unexpected. Moreover, competitive cell-binding assays with LNCap cells showed at least a 2-fold improvement in the IC₅₀ value of DFO-PSMAi-PEG-Cy5-C' dots (IC₅₀ = 1.8 nM), as against that seen for the free PSMAi peptide (IC₅₀ = 4.5 nM), suggesting greater potency of the particle probe (Figure S1).

DFO-PSMAi-PEG-Cy5-C' dots were labeled with ⁸⁹Zr-oxalate (37 °C, 60 min), followed by removal of any unbound ⁸⁹Zr with an EDTA challenge for 60 min, and PD-10 purification.^{23,25} A >70% labeling yield was achieved using a particle/⁸⁹Zr ratio of 0.75 nmol/1 mCi. The specific activity was estimated to be >1000 Ci/mmol, and >99% end-of-synthesis radiochemical purity was found, quantified by radio-iTLC. Figure S2 shows a representative PD-10 elution profile of ⁸⁹Zr-DFO-PSMAi-PEG-Cy5-C' dots; the final product was collected from fraction 2.5 to 4.0 mL. Our results further demonstrated comparable radiochemical stability of ⁸⁹Zr-DFO-PSMAi-PEG-Cy5-C' dots in PBS, murine serum, and human serum at 37 °C for up to 168 h, with final postincubation purities (mean ± SD) of 95.2 ± 1.0%, 96.6 ± 1.7%, and 97.6 ± 0.6%, respectively (Figure 1F).

A metabolic-cage study was performed to quantitatively assess the renal and hepatic clearance rates of ⁸⁹Zr-DFO-PSMAi-PEG-Cy5-C' dots in normal healthy mice (*n* = 3). Each mouse was first intravenously (iv) injected with ~50 μCi of ⁸⁹Zr-DFO-PSMAi-PEG-Cy5-C' dots and housed in a metabolic cage. Urine and fecal specimens were collected separately at 4, 24, 48, 72, 144, and 168 h p.i. and their activities assayed using a CRC-55tR dose calibrator. Figure 2A and Table S1 show the resulting renal and hepatic clearances for ⁸⁹Zr-DFO-PSMAi-PEG-Cy5-C' dots measured over 1 week. Urinary and fecal clearance at 4 h p.i. was found to be 26.4 ± 3.6 percentage of the injected dose (%ID) and less than 0.1 %ID, respectively, yielding a urine-to-fecal clearance ratio >5100 and thus clearly indicating dominant renal clearance at early p.i. time points. Cumulative clearance in both urine and

feces increased to 41.0 ± 4.0 %ID and 11.6 ± 2.5 %ID by 24 h p.i., respectively. As shown in Figure 2A, renal clearance rates subsequently decreased, with the total clearance estimated to be 52.6 ± 4.0 %ID on day 7. Total hepatic clearance of ^{89}Zr -DFO-PSMAi-PEG-Cy5-C' dots was 20.3 ± 1.7 %ID on day 7. The final renal-to-hepatic-clearance ratio was ~ 3 , as shown in Table S1.

To evaluate time-dependent changes in particle biodistributions, we sacrificed mice and collected, wet-weighed, and counted all major organs (Table S2) with a gamma counter after 7 days. Figure 2B and Table S2 present the ex vivo biodistribution data as the %ID of ^{89}Zr -DFO-PSMAi-PEG-Cy5-C' dots in healthy male mice. Besides the dominant accumulation of ^{89}Zr -DFO-PSMAi-PEG-Cy5-C' dots in urine and feces, the respective particle uptakes in liver, spleen, kidneys, and salivary glands were found to be only ~ 1 %ID or less. A more complete biodistribution study, presented as the percentage of the injected dose per gram (%ID/g), was performed in a separate cohort of mice over a range of p.i. time points. As shown in Figure S3 and Table S3, radioactivity was predominantly found in both mouse blood and urine at early p.i. time points. Unlike most other radiolabeled silica nanoparticles exhibiting sizes greater than the renal clearance cutoff and showing high RES accumulations,^{28–36} uptake of our particle probe in all major organs, including liver, kidney, and salivary glands, was found to be ~ 5 %ID/g or less 24 h p.i.. These findings clearly underscore the importance of carefully controlling particle physicochemical properties (i.e., size) to achieve bulk renal clearance and thereby substantially reduce nonspecific accumulations in major healthy organs and tissues.

For estimation of mean organ absorbed doses and particle dosimetry in a 70-kg standard man, biodistribution data (Table S3) were rescaled to a 70-kg body mass, fit to exponential functions, integrated to yield organ ^{89}Zr residence times, and analyzed using the OLINDA program.¹⁷ As shown in Table S4, when compared to that derived for the ^{89}Zr -labeled PSMA-targeted minibody (i.e., ^{89}Zr -IAb2M, MW = 80 kDa)⁷ and intact antibody (i.e., ^{89}Zr -huJ591, MW = 150 kDa),³⁷ our ^{89}Zr -DFO-PSMAi-PEG-Cy5-C' dots showed significantly reduced absorbed doses in traditional dose-limiting organs: kidney (>10 -fold less), liver (>6 -fold less), spleen (>4 -fold less), and red marrow (~ 3 -fold less). These results suggest that ^{89}Zr -DFO-PSMAi-PEG-Cy5-C' dots can overcome the unfavorable biological and dose-limiting properties generally found for larger probes (i.e. >10 nm diameter).

Finally, we investigated in vivo PSMA targeting of ^{89}Zr -DFO-PSMAi-PEG-Cy5-C' dots in LNCap and PC-3 tumor-bearing mice. ^{89}Zr -DFO-PSMAi-PEG-Cy5-C' dots were intravenously injected into LNCap ($n = 5$) and PC-3 ($n = 5$) tumors and the mice imaged sequentially using a Focus 120 microPET scanner (Concorde Microsystems). As shown in Figure 3, significant bladder activity was observed 2 h p.i. for all tumor-bearing mice, while cardiac uptake was estimated to be 17–20 %ID/g, clearly indicating particle in circulation. Significant differences (** $p < 0.005$) in tumor uptake between these cohorts were also observed at all p.i. time points. At 24 h p.i., tumor uptake in LNCap mice was 8.1 ± 1.2 %ID/g, a greater than 2-fold difference over that seen for PC-3 mice (3.9 ± 0.5 %ID/g) (Figure 3 and Figure 4A). Tumor uptake in LNCap mice peaked at 48 h p.i. (~ 9 %ID/g), with retention observed up to 72 h prior to sacrificing mice for biodistribution studies and correlative histology and autoradiography (Figure S4). In addition to noting enhanced target-

specific particle accumulations, LNCap mice exhibited significant differences in tumor-to-blood (4.8 ± 1.1 vs 2.0 ± 0.5 at 72 h p.i., Figure 4B), tumor-to-liver (1.5 ± 0.2 vs 0.7 ± 0.1 at 72 h p.i., Figure 4C), and tumor-to-muscle ratios (12.2 ± 1.8 vs 3.8 ± 0.6) at 72 h p.i., Figure 4D) compared to that of PC-3 mice. Biodistribution findings also showed enhanced tumor uptake in LNCap mice (Figure 4E). Taken together, we successfully maximized targeted delivery, uptake, retention, and tumor-to-background ratios in PSMA-expressing xenografts intravenously injected with the particle tracer, while maintaining predominant renal clearance.

As the long-term goal of these studies is to develop the particle for theranostic (i.e., diagnosis and therapy) applications, it was critically important to collectively improve multiple biological properties in tandem to maximize tumor uptake and minimize off-target accumulations in the salivary glands, reticuloendothelial system, and kidneys, while maintaining a renally clearable product. By carefully tailoring particle physical, surface chemical, and imaging properties, we have readied this PSMA-targeting particle probe for both diagnostic and therapeutic applications and addressed major hurdles that are typically seen with larger-size probes (e.g., dose-limiting toxicity to normal tissues occurring in the setting of radiotherapy).

At the present time, the diagnosis and staging of PCa, along with assessments of treatment response, are largely based on conventional magnetic resonance or CT imaging strategies; ^{99m}Tc -methylene diphosphonate (^{99m}Tc -MDP) scintigraphy is also commonly used for imaging bone metastases. Although PSMA-targeting PET imaging probes, formulated using peptides or monoclonal antibodies, offer attractive alternatives for diagnosing and potentially treating PCa, they continue to face technical hurdles, such as prolonged kinetics and/or high off-target accumulations that can be dose-limiting and reduce efficacy. Furthermore, these probes lack fluorescent dyes and cannot be used in surgical settings to directly visualize or resect disease with optical imaging guidance. By contrast, and while not directly addressed in the current work, the combination of our PSMA-targeting PET/optical C' dot platform with a fluorescence camera system can be used to improve disease detection during image-guided surgery. In current practice, intraoperative guidance has often relied upon the surgeon's visual cues and tactile feedback.

CONCLUSIONS

In conclusion, we developed a first-in-kind ultrasmall, PSMA-targeting dual-modality (PET/optical) imaging platform for prostate cancer care. By carefully controlling the C' dot size and surface chemistry, we were able to demonstrate favorable in vivo pharmacokinetics, bulk renal clearance profiles, and product dosimetry (particularly involving potentially at-risk tissues in a therapeutic setting), while overcoming hurdles (i.e., by minimizing off-target localization) that have limited the utility of peptide-based probes and radioimmunoconjugates targeting PSMA. On the basis of these findings, PSMA-targeting C' dots can be exploited as a highly versatile tool for all phases of prostate cancer management: in vivo scintigraphic imaging, image-guided surgery, treatment planning, and α -/ β -particle targeted radiotherapy.

Supplementary Material

Refer to Web version on PubMed Central for supplementary material.

Funding

This study was funded by grants from the National Institutes of Health (1U54 CA199081-01 to M.B. and U.W.) and Sloan Kettering Institute (Core Grant P30 CA008748CCSG).

REFERENCES

- (1). Siegel RL; Miller KD; Jemal A Cancer statistics, 2019. *Ca-Cancer J. Clin* 2019, 69, 7–34. [PubMed: 30620402]
- (2). Lindenberg L; Choyke P; Dahut W Prostate Cancer Imaging with Novel PET Tracers. *Curr. Urol. Rep* 2016, 17, 18–31. [PubMed: 26874530]
- (3). Wallitt KL; Khan SR; Dubash S; Tam HH; Khan S; Barwick TD Clinical PET Imaging in Prostate Cancer. *Radio-graphics* 2017, 37, 1512–1536.
- (4). Silver DA; Pellicer I; Fair WR; Heston WD; Cordon-Cardo C Prostate-Specific Membrane Antigen Expression in Normal and Malignant Human Tissues. *Clin. Cancer Res* 1997, 3, 81–85. [PubMed: 9815541]
- (5). Bostwick DG; Pacelli A; Blute M; Roche P; Murphy GP Prostate Specific Membrane Antigen Expression in Prostatic Intraepithelial Neoplasia and Adenocarcinoma: A Study of 184 Cases. *Cancer* 1998, 82, 2256–2261. [PubMed: 9610707]
- (6). Pandit-Taskar N; O'Donoghue JA; Durack JC; Lyashchenko SK; Cheal SM; Beylgeril V; Lefkowitz RA; Carrasquillo JA; Martinez DF; Fung AM; Solomon SB; Gonen M; Heller G; Loda M; Nanus DM; Tagawa ST; Feldman JL; Osborne JR; Lewis JS; Reuter VE; Weber WA; Bander NH; Scher HI; Larson SM; Morris MJ A Phase I/II Study for Analytic Validation of ⁸⁹Zr-J591 ImmunoPET as a Molecular Imaging Agent for Metastatic Prostate Cancer. *Clin. Cancer Res* 2015, 21, 5277–5285. [PubMed: 26175541]
- (7). Pandit-Taskar N; O'Donoghue JA; Ruan S; Lyashchenko SK; Carrasquillo JA; Heller G; Martinez DF; Cheal SM; Lewis JS; Fleisher M; Keppler JS; Reiter RE; Wu AM; Weber WA; Scher HI; Larson SM; Morris MJ First-in-Human Imaging with ⁸⁹Zr-Df-IAB2M Anti-PSMA Minibody in Patients with Metastatic Prostate Cancer: Pharmacokinetics, Biodistribution, Dosimetry, and Lesion Uptake. *J. Nucl. Med* 2016, 57, 1858–1864. [PubMed: 27516450]
- (8). Afshar-Oromieh A; Malcher A; Eder M; Eisenhut M; Linhart HG; Hadaschik BA; Holland-Letz T; Giesel FL; Kratochwil C; Haufe S; Haberkorn U; Zechmann CM PET imaging with a [⁶⁸Ga]gallium-labelled PSMA Ligand for the Diagnosis Of Prostate Cancer: Biodistribution in Humans and First Evaluation of Tumour Lesions. *Eur. J. Nucl. Med. Mol. Imaging* 2013, 40, 486–495. [PubMed: 23179945]
- (9). Afshar-Oromieh A; Hetzheim H; Kratochwil C; Benesova M; Eder M; Neels OC; Eisenhut M; Kubler W; Holland-Letz T; Giesel FL; Mier W; Kopka K; Haberkorn U The Theranostic PSMA Ligand PSMA-617 in the Diagnosis of Prostate Cancer by PET/CT: Biodistribution in Humans, Radiation Dosimetry, and First Evaluation of Tumor Lesions. *J. Nucl. Med* 2015, 56, 1697–1705. [PubMed: 26294298]
- (10). Vallabhajosula S; Nikolopoulou A; Jhanwar YS; Kaur G; Tagawa ST; Nanus DM; Bander NH; Goldsmith SJ Radioimmunotherapy of Metastatic Prostate Cancer with (1)(7) (7)Lu-DOTAhuJ591 Anti Prostate Specific Membrane Antigen Specific Monoclonal Antibody. *Curr. Radiopharm* 2015, 9, 44–53.
- (11). Holland JP; Divilov V; Bander NH; Smith-Jones PM; Larson SM; Lewis JS Zr-89-DFO-J591 for ImmunoPET of Prostate-Specific Membrane Antigen Expression In Vivo. *J. Nucl. Med* 2010, 51, 1293–1300. [PubMed: 20660376]
- (12). Oh SW; Cheon GJ Prostate-Specific Membrane Antigen PET Imaging in Prostate Cancer: Opportunities and Challenges. *Korean J. Radiol* 2018, 19, 819–831. [PubMed: 30174470]

- (13). Psimadas D; Valotassiou V; Alexiou S; Tsougos I; Georgoulas P Radiolabeled mAbs as Molecular Imaging and/or Therapy Agents Targeting PSMA. *Cancer Invest.* 2018, 36, 118–128. [PubMed: 29393702]
- (14). Roll W; Bode A; Weckesser M; Bogemann M; Rahbar K Excellent Response to ^{177}Lu -PSMA-617 Radioligand Therapy in a Patient With Advanced Metastatic Castration Resistant Prostate Cancer Evaluated by ^{68}Ga -PSMA PET/CT. *Clin Nucl. Med* 2017, 42, 152–153. [PubMed: 27922871]
- (15). Kratochwil C; Bruchertseifer F; Giesel FL; Weis M; Verburg FA; Mottaghy F; Kopka K; Apostolidis C; Haberkorn U; Morgenstern A ^{225}Ac -PSMA-617 for PSMA-Targeted alpha-Radiation Therapy of Metastatic Castration-Resistant Prostate Cancer. *J. Nucl. Med* 2016, 57, 1941–1944. [PubMed: 27390158]
- (16). Larson DR; Ow H; Vishwasrao HD; Heikal AA; Wiesner U; Webb WW Silica Nanoparticle Architecture Determines Radiative Properties of Encapsulated Fluorophores. *Chem. Mater* 2008, 20, 2677–2684.
- (17). Stabin MG; Sparks RB; Crowe E OLINDA/EXM: the Second-Generation Personal Computer Software for Internal Dose Assessment in Nuclear Medicine. *J. Nucl. Med* 2005, 46, 1023–1027. [PubMed: 15937315]
- (18). Ma K; Mendoza C; Hanson M; Werner-Zwanziger U; Zwanziger J; Wiesner U Control of Ultrasmall Sub-10 nm Ligand-Functionalized Fluorescent Core-Shell Silica Nanoparticle Growth in Water. *Chem. Mater* 2015, 27, 4119–4133.
- (19). Ma K; Zhang D; Cong Y; Wiesner U Elucidating the Mechanism of Silica Nanoparticle PEGylation Processes Using Fluorescence Correlation Spectroscopies. *Chem. Mater* 2016, 28, 1537–1545.
- (20). Ma K; Wiesner U Modular and Orthogonal Post-PEGylation Surface Modifications by Insertion Enabling Penta-Functional Ultrasmall Organic-Silica Hybrid Nanoparticles. *Chem. Mater* 2017, 29, 6840–6855.
- (21). Herz E; Ow H; Bonner D; Burns A; Wiesner U Dye structure-optical property correlations in near-infrared fluorescent core-shell silica nanoparticles. *J. Mater. Chem* 2009, 19, 6341–6347.
- (22). Ow H; Larson DR; Srivastava M; Baird BA; Webb WW; Wiesner U Bright and Stable Core-Shell Fluorescent Silica Nanoparticles. *Nano Lett.* 2005, 5, 113–117. [PubMed: 15792423]
- (23). Chen F; Ma K; Benezra M; Zhang L; Cheal SM; Phillips E; Yoo B; Pauliah M; Overholtzer M; Zanzonico P; Sequeira S; Gonen M; Quinn T; Wiesner U; Bradbury MS Cancer-Targeting Ultrasmall Silica Nanoparticles for Clinical Translation: Physicochemical Structure and Biological Property Correlations. *Chem. Mater* 2017, 29, 8766–8779. [PubMed: 29129959]
- (24). Chen F; Ma K; Zhang L; Madajewski B; Zanzonico P; Sequeira S; Gonen M; Wiesner U; Bradbury MS Target-or-Clear Zirconium-89 Labeled Silica Nanoparticles for Enhanced Cancer-Directed Uptake in Melanoma: A Comparison of Radiolabeling Strategies. *Chem. Mater* 2017, 29, 8269–8281. [PubMed: 29123332]
- (25). Chen F; Ma K; Madajewski B; Zhuang L; Zhang L; Rickert K; Marelli M; Yoo B; Turker MZ; Overholtzer M; Quinn TP; Gonen M; Zanzonico P; Tiesca A; Bowen MA; Norton L; Subramony JA; Wiesner U; Bradbury MS Ultrasmall targeted nanoparticles with engineered antibody fragments for imaging detection of HER2-overexpressing breast cancer. *Nat. Commun* 2018, 9, 4141. [PubMed: 30297810]
- (26). Chen F; Zhang X; Ma K; Madajewski B; Benezra M; Zhang L; Phillips E; Turker MZ; Gallazzi F; Penate-Medina O; Overholtzer M; Pauliah M; Gonen M; Zanzonico P; Wiesner U; Bradbury MS; Quinn TP Melanocortin-1 Receptor-Targeting Ultrasmall Silica Nanoparticles for Dual-Modality Human Melanoma Imaging. *ACS Appl. Mater. Interfaces* 2018, 10, 4379–4393. [PubMed: 29058865]
- (27). Taylor RM; Severns V; Brown DC; Bisoffi M; Sillerud LO Prostate Cancer Targeting Motifs: Expression of Alphanu Beta3, Neurotensin Receptor 1, Prostate Specific Membrane Antigen, and Prostate Stem Cell Antigen in Human Prostate Cancer Cell Lines And Xenografts. *Prostate* 2012, 72, 523–532. [PubMed: 21748756]
- (28). Chen F; Goel S; Valdovinos HF; Luo H; Hernandez R; Barnhart TE; Cai W In Vivo Integrity and Biological Fate of Chelator-Free Zirconium-89-Labeled Mesoporous Silica Nanoparticles. *ACS Nano* 2015, 9, 7950–7959. [PubMed: 26213260]

- (29). Chen F; Hong H; Goel S; Graves SA; Orbay H; Ehlerding EB; Shi S; Theuer CP; Nickles RJ; Cai W In Vivo Tumor Vasculature Targeting of CuS@MSN Based Theranostic Nanomedicine. *ACS Nano* 2015, 9, 3926–3934. [PubMed: 25843647]
- (30). Chen F; Hong H; Zhang Y; Valdovinos HF; Shi S; Kwon GS; Theuer CP; Barnhart TE; Cai W In Vivo Tumor Targeting and Image-Guided Drug Delivery with Antibody-Conjugated, Radiolabeled Mesoporous Silica Nanoparticles. *ACS Nano* 2013, 7, 9027–9039. [PubMed: 24083623]
- (31). Chen F; Valdovinos HF; Hernandez R; Goel S; Barnhart TE; Cai W Intrinsic Radiolabeling of Titanium-45 using Mesoporous Silica Nanoparticles. *Acta Pharmacol. Sin* 2017, 38, 907–913. [PubMed: 28414201]
- (32). Goel S; Ferreira CA; Chen F; Ellison PA; Siamof CM; Barnhart TE; Cai W Activatable Hybrid Nanotheranostics for Tetramodal Imaging and Synergistic Photothermal/Photodynamic Therapy. *Adv. Mater* 2018, 30, 1704367–1704376.
- (33). Goel S; Chen F; Luan S; Valdovinos HF; Shi S; Graves SA; Ai F; Barnhart TE; Theuer CP; Cai W Engineering Intrinsically Zirconium-89 Radiolabeled Self-Destructing Mesoporous Silica Nanostructures for In Vivo Biodistribution and Tumor Targeting Studies. *Adv. Sci. (Weinh)* 2016, 3, 1600122–1600133. [PubMed: 27980987]
- (34). Xu C; Chen F; Valdovinos HF; Jiang D; Goel S; Yu B; Sun H; Barnhart TE; Moon JJ; Cai W Bacteria-Like Mesoporous Silica-Coated Gold Nanorods for Positron Emission Tomography and Photoacoustic Imaging-Guided Chemo-Photo-thermal Combined Therapy. *Biomaterials* 2018, 165, 56–65. [PubMed: 29501970]
- (35). Chen F; Goel S; Shi S; Barnhart TE; Lan X; Cai W General Synthesis of Silica-Based Yolk/Shell Hybrid Nanomaterials and In Vivo Tumor Vasculature Targeting. *Nano Res.* 2018, 11, 4890–4904. [PubMed: 30410684]
- (36). Chen F; Hong H; Shi S; Goel S; Valdovinos HF; Hernandez R; Theuer CP; Barnhart TE; Cai W Engineering of Hollow Mesoporous Silica Nanoparticles for Remarkably Enhanced Tumor Active Targeting Efficacy. *Sci. Rep* 2015, 4, 5080.
- (37). Pandit-Taskar N; O'Donoghue JA; Beylgeril V; Lyashchenko S; Ruan S; Solomon SB; Durack JC; Carrasquillo JA; Lefkowitz RA; Gonen M; Lewis JS; Holland JP; Cheal SM; Reuter VE; Osborne JR; Loda MF; Smith-Jones PM; Weber WA; Bander NH; Scher HI; Morris MJ; Larson SM ⁸⁹Zr-huJ591 Immuno-PET Imaging in Patients with Advanced Metastatic Prostate Cancer. *Eur. J. Nucl. Med. Mol. Imaging* 2014, 41, 2093–2105. [PubMed: 25143071]

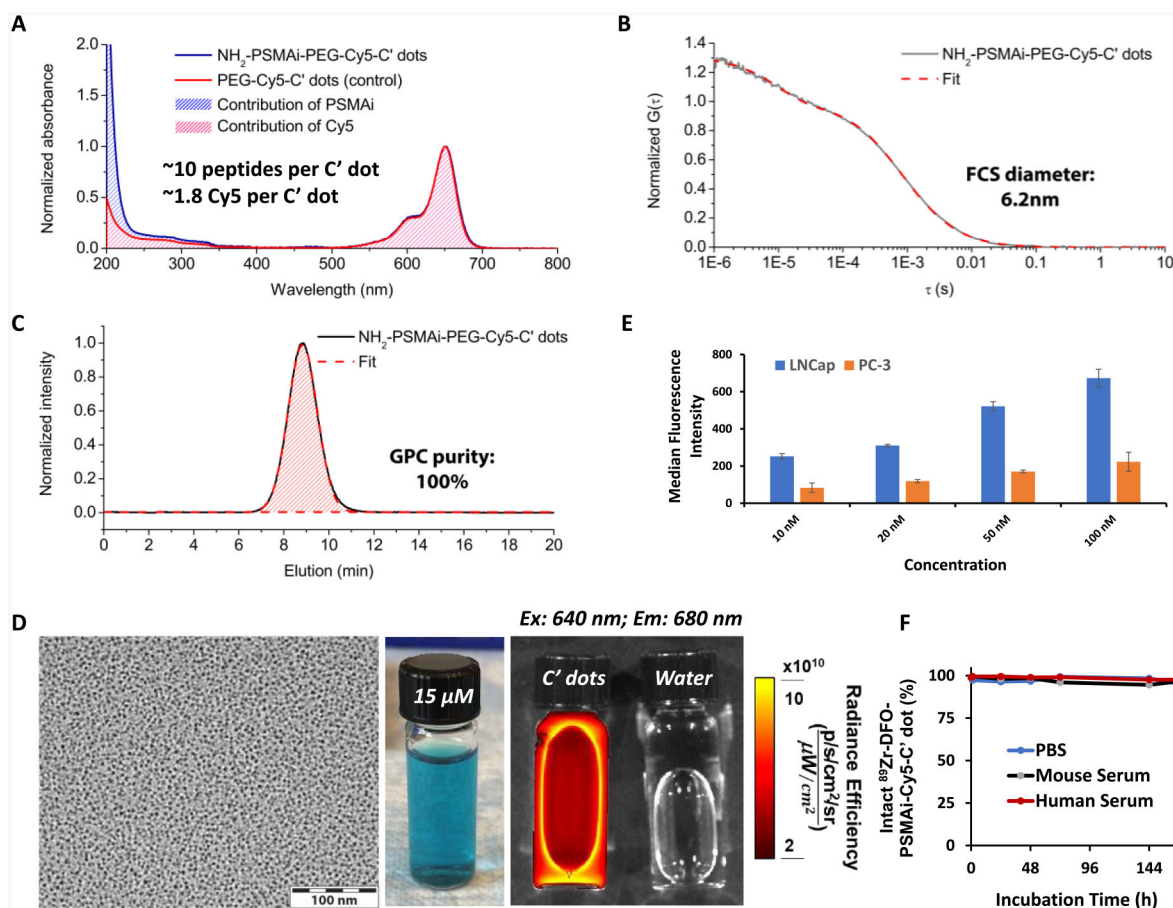


Figure 1.

Characterization of PSMA-targeted C' dots. (A) UV-vis absorbance spectra of NH₂-PSMAi-PEG-Cy5-C' dots (blue line) as compared to PEG-Cy5-C' dots (red line). (B) FCS correlation curve of NH₂-PSMAi-PEG-Cy5-C' dots. Particle size was estimated to be 6.2 nm from FCS fit. (C) GPC elugram confirmed the high purity of NH₂-PSMAi-PEG-Cy5-C' dots after purification step. (D) Left: A representative TEM image of NH₂-PSMAi-PEG-Cy5-C' dots. Middle: A photograph of NH₂-PSMAi-PEG-Cy5-C' dots in water under natural light. Right: The IVIS Spectrum imaging of NH₂-PSMAi-PEG-Cy5-C' dots (left) and water (control, right) under the excitation of 640 nm light (emission filter was set to 680 nm). (E) Cellular binding of DFO-PSMAi-PEG-Cy5-C' dots to LNCap (PSMA-positive) and PC-3 (PSMA-negative) cell lines. (F) In vitro radiostability of ⁸⁹Zr-DFO-PSMAi-PEG-Cy5-C' dots incubated at 37 °C (under shaking, 650 rpm) in PBS (blue line), mouse serum (black line), and human serum (red line).

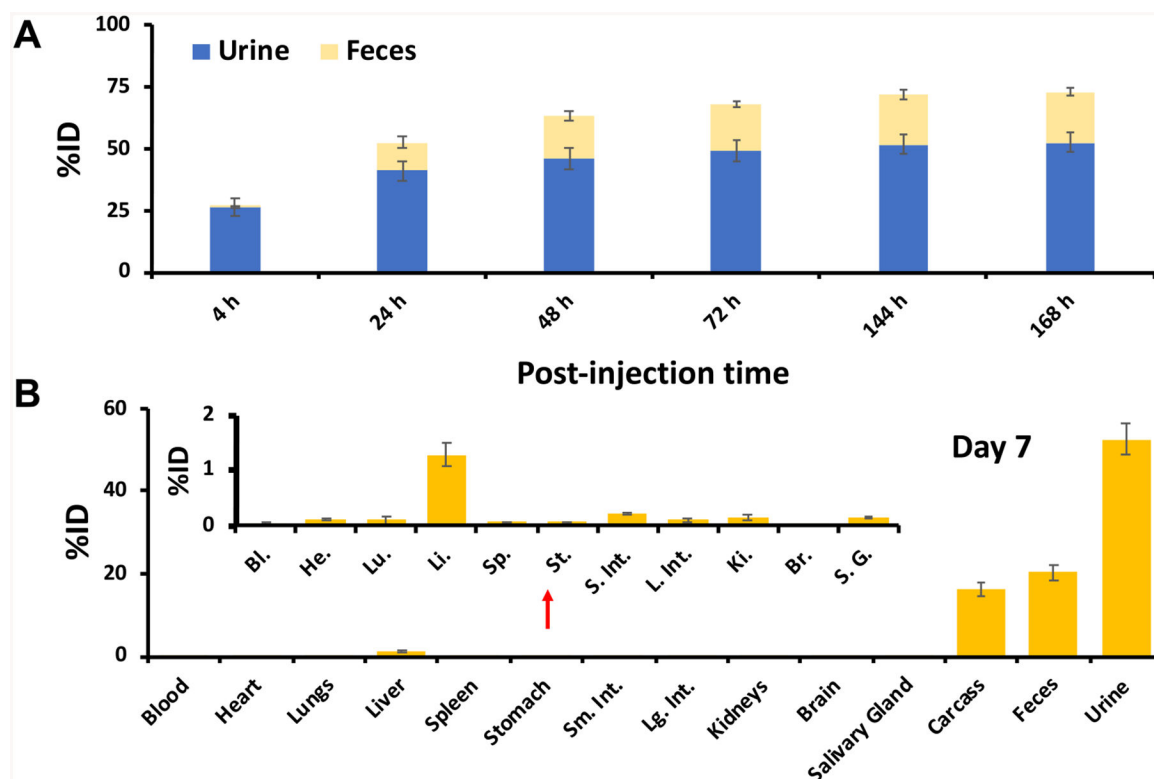


Figure 2. Renal/hepatic clearance and biodistribution of ^{89}Zr -DFO-PSMAi-PEG-Cy5-C' dots in healthy male mice after intravenous administration. (A) Cumulative clearance measurements of ^{89}Zr -DFO-PSMAi-PEG-Cy5-C' dots in urine and feces at various p.i. time points ($n = 3$; error bars: mean \pm SD). (B) Biodistribution of ^{89}Zr -DFO-PSMAi-PEG-Cy5-C' dots in major organs and tissues, expressed in terms of %ID, on day 7 p.i. ($n = 3$; error bars: mean \pm SD). The carcass activity represents the activity in the total body once the organs specified and have been removed and assayed separately.

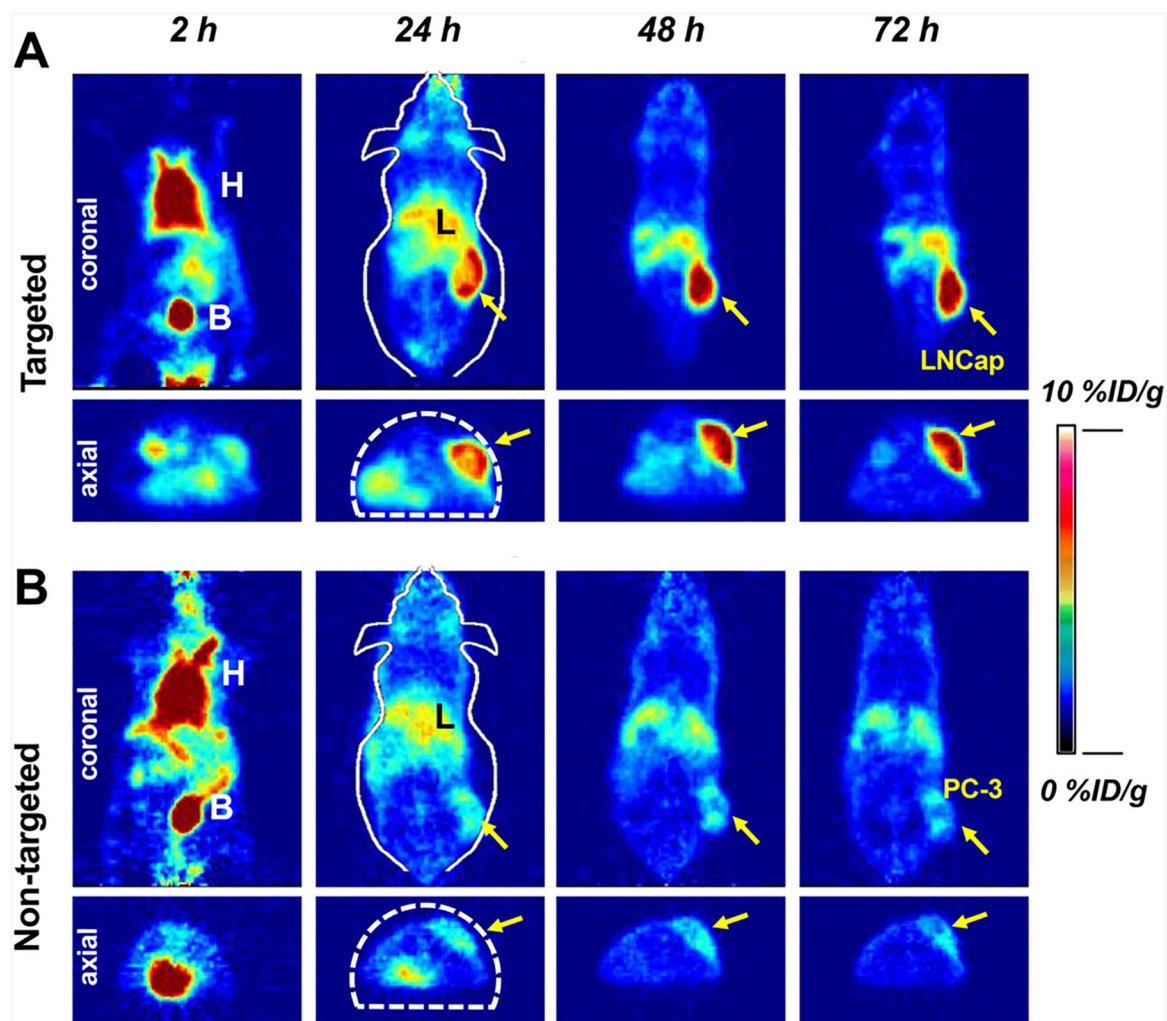


Figure 3. In vivo cancer-targeted PET imaging of ^{89}Zr -DFO-PSMAi-PEG-Cy5-C' dots intravenously injected into (A) LNCap, targeted group, and (B) PC-3, nontargeted group, tumor-bearing mice. H: heart; B: bladder; L: liver. Both LNCap and PC-3 tumors were marked with yellow arrows.

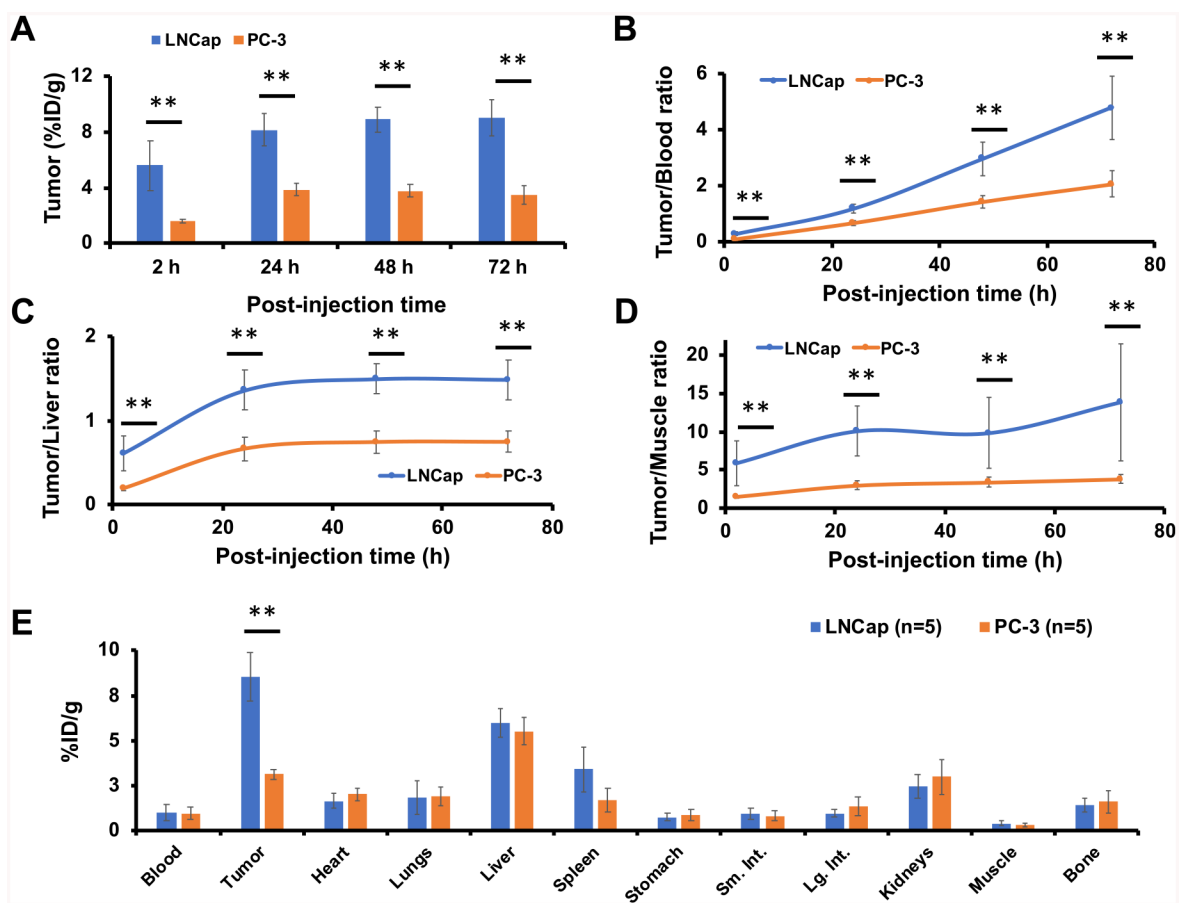
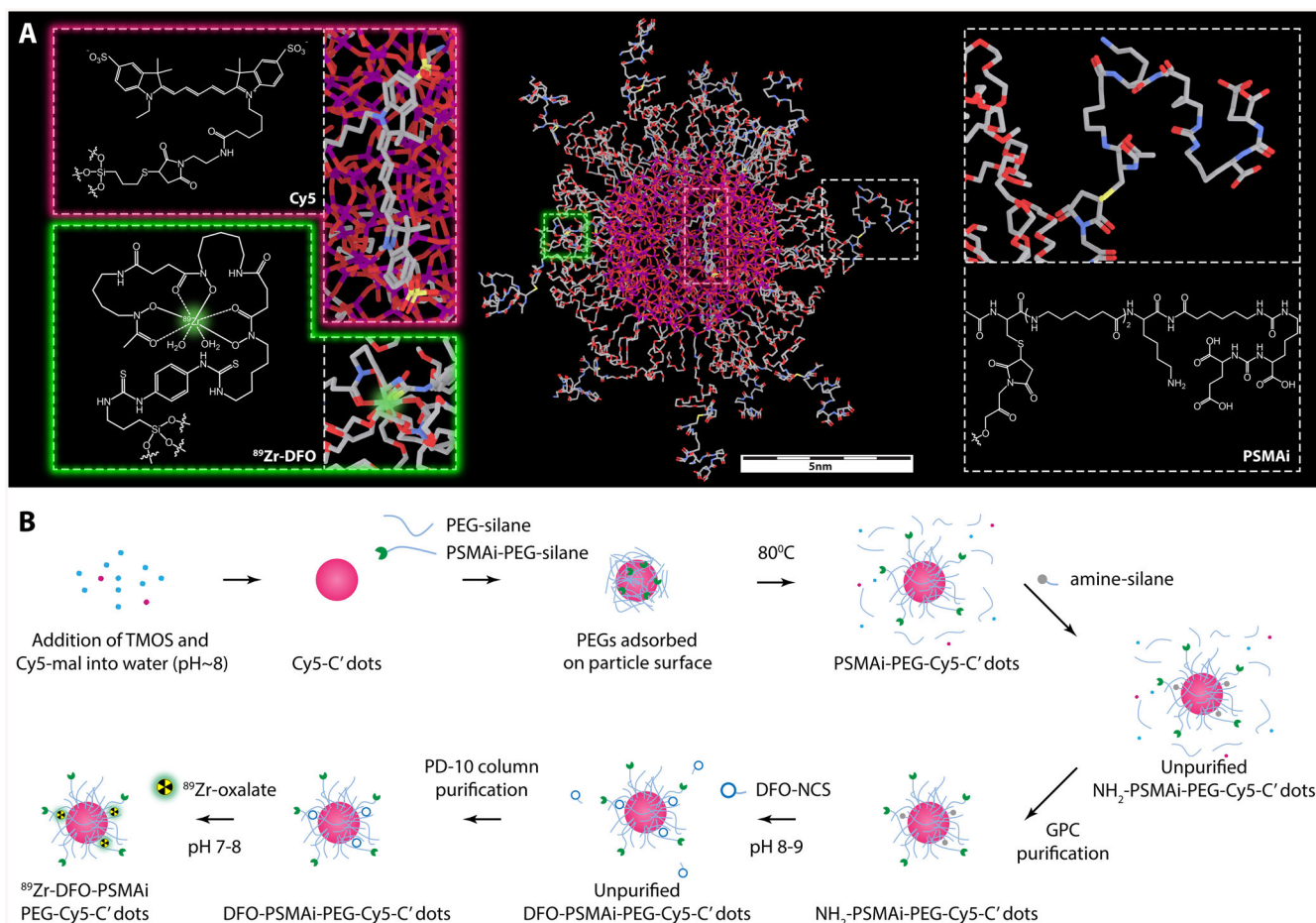


Figure 4. Region-of-interest quantification and biodistribution studies. Comparison of (A) tumor uptake, (B) tumor-to-blood ratios, (C) tumor-to-liver ratios, and (D) tumor-to-muscle ratios between targeted (LNCap) and nontargeted (PC-3) cohorts ($n = 5$ for each group). (E) Biodistribution of ^{89}Zr -DFO-PSMAi-PEG-Cy5-C' dots in LNCap or PC-3 tumor-bearing mice at 72 h p.i. (** $p < 0.005$).



Scheme 1. (A) Three-Dimensional (3D) Rendering of Core-Shell Structured ^{89}Zr -DFO-PSMAi-PEG-Cy5-C' Dot Prostate Cancer-Specific Targeting Probe;^a (B) Schematic Illustration Showing the Synthesis of ^{89}Zr -DFO-PSMAi-PEG-Cy5-C' Dots^b

^aThe core of the nanoparticle is a Cy5 dye-encapsulating silica scaffold with its physical size controlled to be around 3–4 nm. The shell includes a protective layer of short PEG chains (MW: ~500 g/mol), radionuclide chelators, DFO, for ^{89}Zr labeling, and PSMAi peptides for active PCa targeting. ^bCy5-silane was reacted with TMOS in DI water at room temperature with the pH adjusted to ~8 to form Cy5-C' dots. Then PEGylation and peptide-functionalization steps were introduced to form PSMAi-PEG-Cy5-C' dots. As-synthesized PSMAi-PEG-Cy5-C' dots were then surface-functionalized with amine groups by reacting with amine-silanes to form NH_2 -PSMAi-PEG-Cy5-C' dots. The GPC-purified NH_2 -PSMAi-PEG-Cy5-C' dots were mixed with DFO-NCS to form DFO-PSMAi-PEG-Cy5-C' dots. Finally, ^{89}Zr was attached to form ^{89}Zr -DFO-PSMAi-PEG-Cy5-C' dots.